ANIMAL ROBOTS

A cellular platform for the development of synthetic living machines

Douglas Blackiston[1]*, Emma Lederer[1]*, Sam Kriegman[2], Simon Garnier[3], Joshua Bongard[2], Michael Levin[1,4†]

Robot swarms have, to date, been constructed from artificial materials. Motile biological constructs have been created from muscle cells grown on precisely shaped scaffolds. However, the exploitation of emergent self-organization and functional plasticity into a self-directed living machine has remained a major challenge. We report here a method for generation of in vitro biological robots from frog (*Xenopus laevis*) cells. These xenobots exhibit coordinated locomotion via cilia present on their surface. These cilia arise through normal tissue patterning and do not require complicated construction methods or genomic editing, making production amenable to high-throughput projects. The biological robots arise by cellular self-organization and do not require scaffolds or microprinting; the amphibian cells are highly amenable to surgical, genetic, chemical, and optical stimulation during the self-assembly process. We show that the xenobots can navigate aqueous environments in diverse ways, heal after damage, and show emergent group behaviors. We constructed a computational model to predict useful collective behaviors that can be elicited from a xenobot swarm. In addition, we provide proof of principle for a writable molecular memory using a photoconvertible protein that can record exposure to a specific wavelength of light. Together, these results introduce a platform that can be used to study many aspects of self-assembly, swarm behavior, and synthetic bioengineering, as well as provide versatile, soft-body living machines for numerous practical applications in biomedicine and the environment.

INTRODUCTION

Constructing robot swarms at small scales remains an open problem (*1*–*4*). Fabrication challenges abound, yet manufacturing advances are allowing for the construction of large numbers of microrobots composed of diverse components (*5*–*7*). Formulating and programming complex control policies into very small devices to enable swarm behavior also raises many conceptual challenges (*8*–*10*). However, recent advances in synthetic biology suggest an alternative path to many-bodied microswarms that, to some degree, sidestep some of these manufacturing and conceptual challenges: constructing small-scale living machines solely from biological tissue (*11*) in such a way that they inherit the adaptive potential of their wild-type analogs. All organisms, including those that grow to macro-size scales, pass through early stages of development in which they must achieve and maintain complex behaviors. This raises the possibility of direct and indirect perturbations to natural development, including tissue explantation (the isolation and culture of developing tissues) and/or rearrangement, to achieve stable small-scale biological forms orthogonal to any found in nature. One major advantage of this approach is that living cells already have numerous sensors, effectors, and signaling/computational circuits. Their native biochemical, biomechanical, and bioelectrical communication and control machinery can be repurposed for novel functionality (i.e., functionality that the source organism cannot not perform) and does not have to be directly engineered.

Classical developmental biology has long focused on uncovering the genes, organizing centers, and signaling cascades that drive specification of cells and tissues from undifferentiated precursors (*12*, *13*). Historically, this research used in vivo embryonic models to examine the effects of misexpression of early patterning genes on downstream phenotypes, creating morphological and molecular fate maps in their respective native systems (*14*–*19*). A more recent effort has been directed toward harnessing the information garnered from this classical, basic biology to create complex systems from the ground up in vitro. These biological robots allow investigation into diverse topics ranging from the origin of multicellularity, aspects of basal cognition, synthetic morphology, and the creation of implantable bio-prosthetics.

A recognizable example of this methodology is organoids, three-dimensional in vitro cultured representations of complex tissues and organs that reproduce the physiology of their in vivo counterparts. This work has revealed many mechanisms of stem cell differentiation and has enabled investigators to drive progenitor cells to a wide array of complex tissue types with diverse anatomies, including components of the eye, cerebral structures, gut, liver, intestine, mammary gland, kidney, and pancreas among others (*20*). Furthermore, recent advances led to the miniaturization and daisy-chaining of multiple organoid types, leading to body-on-a-chip systems aimed at recapitulating whole-organism nested physiology (*21*, *22*). The power of this technology enables investigators to model complex multiorgan diseases, understand drug interactions between organ systems, and better represent patient physiology compared with single organoids grown in culture. However, although these techniques further our understanding of many aspects of differentiation and self-assembly, they are designed to replicate existing in vivo systems rather than building unconventional morphologies. Moreover, they are largely produced by micromanaging (via bioprinting or scaffolds) cellular arrangement and have yet to truly

[1]Allen Discovery Center at Tufts University, Medford, MA 02155, USA. [2]Department of Computer Science, University of Vermont, Burlington, VT 05405, USA. [3]Federated Department of Biological Sciences, New Jersey Institute of Technology, Newark, NJ 07102, USA. [4]Wyss Institute for Biologically Inspired Engineering, Harvard University, Boston, MA 02115, USA.
*These authors contributed equally to this work.
†Corresponding author. Email: michael.levin@tufts.edu

exploit the self-assembly and plasticity of cells in vivo (*23*). Similarly, they have not yet been explored for the abilities to exhibit motility and to interact with changing environments. These important advances would enable the extension of physiological and biomedical studies into the emerging field of basal cognition, which seeks to address the origin of computation, decision-making, and adaptive control in diverse body plans. Developing amenable platforms for addressing this question is as crucial for understanding the evolution of brain-body complexity as they are for providing insight and biological inspiration for robotics and artificial intelligence.

Creation of alternative biological forms and structures is the goal of the emerging field of biorobotics. So far, efforts in this field have somewhat coalesced around biohybrid designs, combining synthetic scaffolds or components alongside living cells and tissues. These systems often use muscle actuators to drive rigid artificial body parts, as in the case of a phototaxis-guided biohybrid stingray (*24*), walking and swimming micro-biohybrids propelled by skeletal and cardiac muscle tissue (*25*, *26*), and a macroscale sea turtle–like *Aplysia* biohybrid (*27*). This design approach capitalizes on the benefits of traditional robotics; synthetic components can be modeled quickly in simulation, adjusted, and fabricated with a high degree of precision. It also enables the creation of morphologies that would be difficult or impossible to produce with living tissues, including micrometer-thin sheets with high rigidity, thin filaments resistant to breaking, and sharp edges. However, these synthetic components also contain the limitations of traditional robotic systems—they are unable to regenerate or self-repair, do not have metabolic pathways, and are generally unable to undergo extensive remodeling or migration like living cells and tissues.

Instead of relying on synthetic components that specify the types of function the robot can accomplish, one could take advantage of the plasticity that biology has to offer and build designs entirely out of cells and tissues, creating a fully biological machine (*11*). By using a combination of epidermal and cardiac muscle tissue, one can create fully biological robots that can crawl through aqueous environments, collect debris in their immediate vicinity, quickly heal from mechanical lacerations, and respond to changes in their environment. Robots composed entirely of biological tissue are also completely self-powered, surviving 10 days without additional nutrients, and are fully biodegradable, harmlessly breaking down at their end of life.

The current study expands on these fully biological machines, documenting a bottom-up approach to produce synthetic living machines from cells of the frog *Xenopus laevis*. We hypothesized that when liberated from the rest of the animal, cells could self-organize into a functional morphology that was distinct from their genomically specified default. We report here that tissue explanted from wild-type frog embryos forms synthetic constructs with fascinating morphology and behavior that are different from those of normal tadpoles. These "xenobots" generate swimming motion through the beating of multiciliated cells present on their surface (repurposed machinery whose normal function is to distribute mucus and flow pathogens and other material off the skin). As opposed to imposing tissue placement and shape from the top down (*11*), the design method presented here uses whole explants from developing frog embryos. Although these explants, known as animal caps, have been used for decades to understand the early patterning events of epidermal and neural cell lineages (*28*–*31*), they have not been examined for behavioral capacity as proto-organisms or used to create living machines with specific functions.

Here, we report the use of *Xenopus* animal cells for generating swimming automata that are capable of locomoting through a variety of environments. In addition to categorizing their life cycle, behavior, and regenerative capacity, we also document the ability to introduce simple read-write functionality via RNA-encoded photoconvertible proteins, serving as a proof of principle that experiences can be encoded as a molecular memory and retrieved at a later time. We use computational modeling to explain their multiscale behaviors and effects on their environment. These findings demonstrate that diverse behaviors can be elicited from living machines. Such constructs exhibit characteristic emergent multicellular morphologies, with useful behaviors exhibited by many organisms, such as robustness to damage, exploratory motile behavior, and a spontaneous drive to exhibit collective behavior. This may, in the future, make coaxing desired collective behaviors from xenobot swarms more straightforward than programming equivalent behaviors into swarms of microrobots. Together, these results contribute to an emerging field at the intersection of synthetic biology and developmental biology and represent a highly tractable method to produce simple biological machines.

RESULTS

Xenopus embryonic ectoderm creates a motile living machine

Previous reports used a top-down approach to impose shape, cell type, and contractile motion on a first generation of mobile living machines (*11*). In contrast, the current study used a bottom-up approach to ask whether cells removed from their normal developmental constraints would be able to self-organize into a different type of living form. Production began by harvesting stem cell tissue from the animal hemisphere, a region of undifferentiated presumptive ectoderm, from Neiuwkoop and Faber stage 9 *X. laevis* embryos (Fig. 1A). Tissue explants were then moved to a 0.75× Marc's modified Ringer's (MMR) solution (pH 7.8), allowed to heal for 1 hour at 20°C (Fig. 1B), and cultured at 14°C until experimentation began (Fig. 1D). Under these conditions, explants formed into spheres of tissue (Fig. 1C) composed of 3026 ± 180 cells that differentiated over the course of 4 days into ciliated epithelium. Three days after formation, explants became mobile in aqueous solutions and capable of moving at rates exceeding 100 μm/s (Fig. 1E). Fully differentiated spheres ranged in size from an average of 487 ± 39 μm for the smallest cut explants to 602 ± 30 μm for the largest (n = 15 and 13, respectively).

We observed motile behavior because the cells' native cilia, which normally move material past the animal surface, were repurposed for locomotion. Movement was driven by flow arising from multiciliated cells present on the surface of the construct (which are revealed by anti-acetylated tubulin immunohistochemistry; (Fig. 1F). Further, this motion could be abolished by inhibiting multiciliated cell formation through overexpression of the Notch receptor intracellular domain (NotchICD), which drives the differentiating tissue to other epidermal cell fates (Fig. 1F'). Multiciliated cells were also naturally present on the skin of the frog (Fig. 1G) and likewise responded to the overexpression of NotchICD (Fig. 1G'), although explants displayed a higher multiciliated cell density per area than age-matched tadpoles (Fig. 1H).

The degree of behavioral complexity we observed is normally associated with a nervous system (*32*). Although made entirely of

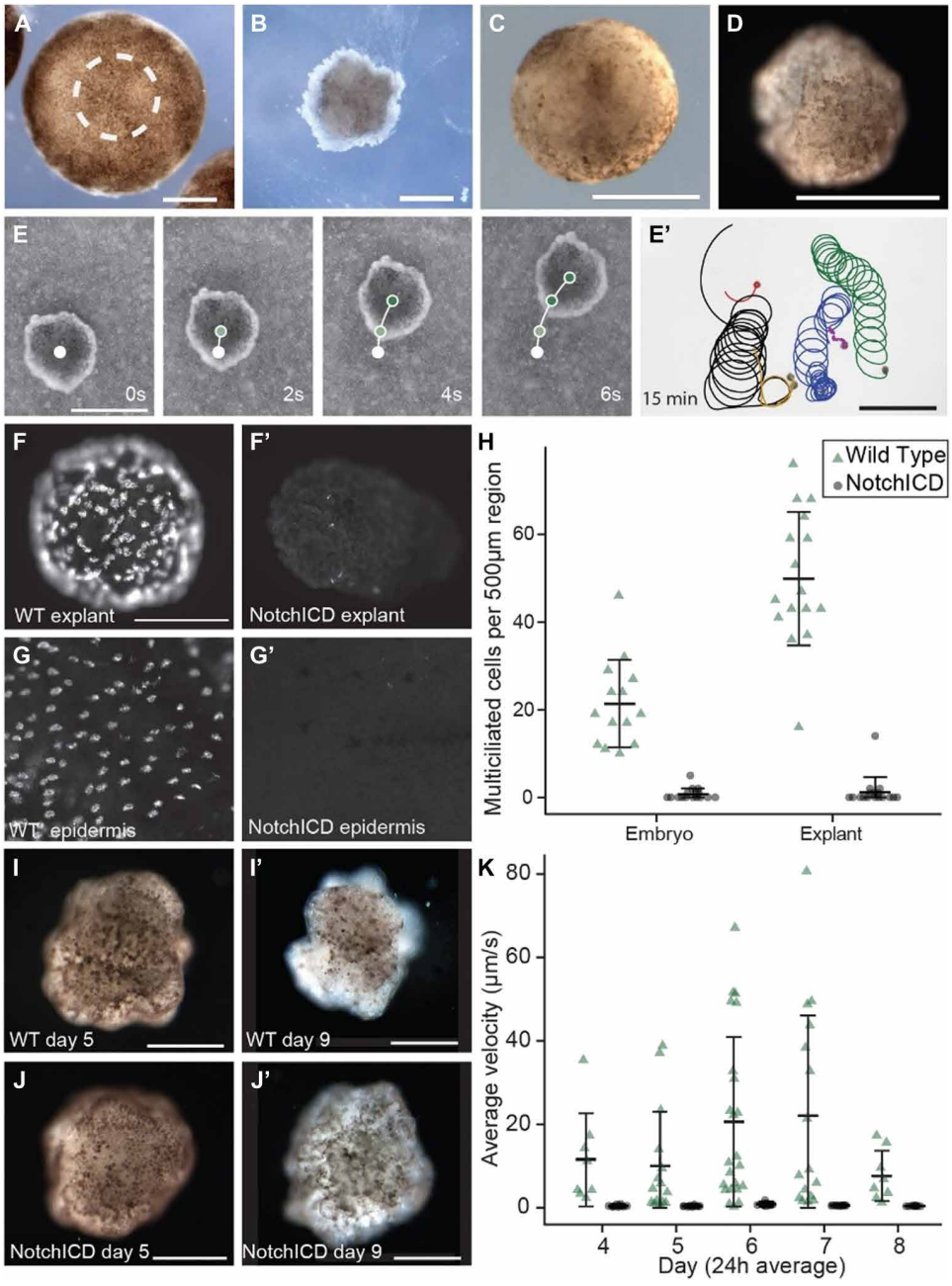

Fig. 1. *Xenopus* embryonic explants create a mobile living machine. (**A**) Tissue is harvested from the animal hemisphere of a Nieuwkoop and Faber stage 9 *X. laevis* embryo. (**B**) Explants are then moved to a 0.75× MMR solution and inverted during healing. (**C**) After 30 min, explants heal into a spherical ball of presumptive ectoderm. (**D**) Four days after formation, explants differentiate into irregular epidermis and are selected for experimentation. (**E**) Time-lapse imaging reveals that explants are mobile when observed in an aqueous environment, with rotational biases observed when tracked for longer time periods (E'). (**F**) Motion is produced by multiciliated cells present on the surface of the explant, visualized with anti-acetylated tubulin immunohistochemistry, and multiciliated cell differentiation can be removed through the overexpression of the NotchICD (F'). (**G**) Multiciliated cells are also present on the epidermis of age-matched embryos and can likewise be inhibited through overexpression of NotchICD (G'). Quantification of multiciliated cells per 500 μM diameter region under each of the conditions (**H**). Both wild-type (**I** and I') and NotchICD-expressing explants (**J** and J') have a life span of about 9 days in standard 0.75× MMR, with movement observed across all days of testing for wild-type explants. Error bars indicate ±1 SD. Scale bars, 500 μM.

skin, we sought to confirm whether there might be any neurons in the xenobots. Using a pan-neuronal marker in immunohistochemistry, we showed that no neurons were present at the surface or internally in any of the individuals imaged (n = 24; fig. S1), indicating that their behavior is driven entirely by the signaling and functional dynamics of non-neural cells. The xenobots are thus a synthetic model for understanding preneural life forms and their capacities (*33*, *34*).

Explants have a life span of about 9 to 10 days after formation and do not require an external food source because they metabolize the maternally loaded yolk platelets present in all early embryonic *Xenopus* tissues. Although their spontaneous disintegration is a welcome safety feature for deploying xenobots, we sought methods to extend their working capacity by taking advantage of the cells' metabolic machinery. We found that their life span can be extended for timeframes exceeding 90 days if raised in a *Xenopus*-specific culture media (fig. S2). This ability to control their life span also availed us of the opportunity to characterize their unique "developmental sequence," because their morphology is not like that of normal *Xenopus* embryos. We found that their pigmentation lightens with age (Fig. 1, I to J'), although their average velocity does not vary significantly across explant life span [Kruskal-Wallis one-way analysis of variance (ANOVA), P = 0.29; Fig. 1K], and they eventually acquire a balloon-like, extended spheroid morphology (fig. S2). Doubling the size of xenobots significantly reduced their average velocity (Student's t test, P = 0.04), likely due to a decreased surface-to-volume ratio. At the end of their life span, explants began shedding cells and deteriorated until the multiciliated cells no longer functioned and the tissue disintegrated. Together, these results demonstrate that embryonic explants from genomically normal *Xenopus* cells form motile living machines with distinct morphologies that are capable of aqueous locomotion via cilia.

Discrete movement types are provided by ciliary alignment and activity

Xenobot locomotion is provided via cilia actuators that produce polarized fluid

flow, thus enabling the diverse behaviors observed as xenobots traverse their aqueous environment. We examined both cell-level and tissue-wide cilia polarization to begin to understand the structural aspects that guide xenobot motion. At the single-cell level, more than 100 individual cilia are present along the apical cell surface, which must coordinate to generate directional fluid movement. Within-cell polarity was visualized using fusion proteins that label separate components of the cilium machinery: CLAMP–green fluorescent protein (GFP), which identifies the rootlet, and centrin–red fluorescent protein (RFP), a marker for the basal body (Fig. 2A) (*35*, *36*). Fluorescent microscopy of these two proteins demonstrated that individual cilia within a single multiciliated cell are highly aligned (yellow arrow, Fig. 2B), an observation that matches previous reports of cilia polarity in *Xenopus* tadpole epidermis (*37*), the base construction material for an individual xenobot.

Tissue-wide cilia flow must be measured across the entire spheroid as it moves through an aqueous environment, necessitating a larger-scale visualization approach. To examine how groups of multiciliated cells generate sufficient flow to move a xenobot, individuals were placed in an aqueous environment containing carmine dye particles (Fig. 2C). The flow generated by the xenobot was then measured and quantified through particle image velocimetry (PIV), a technique that produces displacement vectors based on particulate movement across an observation period. Xenobots with linear movement trajectories demonstrated bilateral flow across opposing lateral surfaces (Fig. 2C), whereas those that were idle or rotating along their central axis showed circular and/or disorganized flow patterns.

To quantitatively profile the different motile behaviors of xenobots, we analyzed 12 hours of xenobot movement recordings ($n = 8$ individuals, 345,592 unique positions) using a cross-entropy clustering algorithm that classified 30-s observation blocks into four discrete behavioral states: (i) linear/wide arcing movement, (ii) circular movement, (iii) an intermediate class between (i) and (ii), and (iv) inactive (Fig. 2D). These data were used to construct a state transition diagram, which indicates the probability with which a xenobot is likely to transition from one behavioral state to another. Idle and circling individuals overwhelmingly maintain their current behaviors (<5% chance to change movement states), whereas those moving linearly are more likely to change to another type of motion (Fig. 2D). This is not unexpected because linear motion cannot continue indefinitely—eventually, any xenobot reaches the edge of the arena where it must stop or turn. Together, these results indicate that individual xenobots display discrete movement patterns resulting from cilia alignment established early in their development. This behavioral characterization forms a baseline of spontaneous exploratory behavior upon which synthetic control circuitry can be imposed in future work.

Xenobots self-repair after damage

A desired feature in biological and artificial machines is a robust ability to deal with unexpected damage arising from both normal wear and tear and external environmental insult. To examine the repair ability of xenobots, 5-day-old individuals were given severe mechanical lacerations with surgical forceps. Lacerations were performed with a single incision, opening a wound across about half of the diameter of the individual and spanning the entire width. Images were collected before damage; directly proceeding damage; 5, 10, and 15 min after damage; and 48 hours after injury. In all cases, individuals were capable of resolving the wound, closing the injury site, and reestablishing a spherical shape (Fig. 3A). Repair appeared to occur quickly, with most of the laceration closing within the first 5 min of observation. After insult, each xenobot was reared individually for an additional 48 hours to determine long-term survival. In no cases was mortality observed; all individuals ($n = 15$) persisted for the remainder of the experiment.

To quantify the degree to which the postrepair shape matched that of the individual before injury, the geometry of an injured xenobot was compared with its initial shape using Hausdorff distances—a calculation of the degree to which two metric spaces differ. Images were first binarized using edge detection software (Fig. 3B) and then run through a Hausdorff distance software, comparing preinjury shapes to each of the subsequent images (Fig. 3C). Analysis revealed that all repair time points showed significant improvement compared with initial injury (repeated-measures ANOVA, $P < 0.0001$), with values remaining flat after the initial 5-min time point. A slight nonsignificant increase can be noted after 48 hours of repair; however, this is likely due to further aging and development (thus further changing xenobot shape compared with the preinjury time point) rather than a regression in repair. Together, these data demonstrate that xenobots have a robust ability to self-repair after injury and that, unlike *Xenopus* tadpoles that repair deformations back to a normal frog-like anatomy (*38*), they repair to their characteristic xenobot morphology, not to a frog embryo–specific shape.

Fluorescent reporters enable a retrievable record of xenobot experience

In addition to exploring an aqueous environment, a valuable capability of a living machine would be the ability to store and recall experiences across the organism's life span. To develop a proof of principle for a generalizable read/write function in xenobots, mRNA encoding the fluorescent reporter EosFP (*39*) was injected into each of four cells of a stage 3 embryo, before tissue excision. When expressed, this reporter emits strong green fluorescence, which is stable over the course of a xenobot life span. However, when exposed to 390-nm blue light, the backbone of the chromophore undergoes a permanent conformational change, shifting the emission wavelength to red. This switch serves as a "write" function of optical experience that can be "read" later by an observer through fluorescent detection. After expressing this construct in xenobots through mRNA microinjection, fluorescence was observed in the green channel but not the red channel before blue light exposure (Fig. 4A). Upon increasing duration exposure to 400-nm light, fluorescence in the green channel decreased, whereas that in the red channel increased, with total photoconversion occurring within 2 min (Fig. 4B). This red signal remained stable over the life span remaining of the xenobot, although green emission did reappear over time due to additional protein translation from the mRNA after the photoconversion period.

To demonstrate that this protein could be used as a record of experience in an unsupervised environment, 10 xenobots expressing the construct were released into a 5-cm-diameter arena (Fig. 4C). On the far side of the arena, 20 mm away from the loading zone, an illuminated 7-mm-diameter spot of 400-nm 0.6-mW blue light was projected vertically through the dish. The xenobots were then given 2 hours to explore their environment, after which, the light source was removed and the xenobots placed in a dark 14°C incubator. Two days after exploring the environment, the xenobots were imaged for fluorescence using fluorescein isothiocyanate and tetramethyl

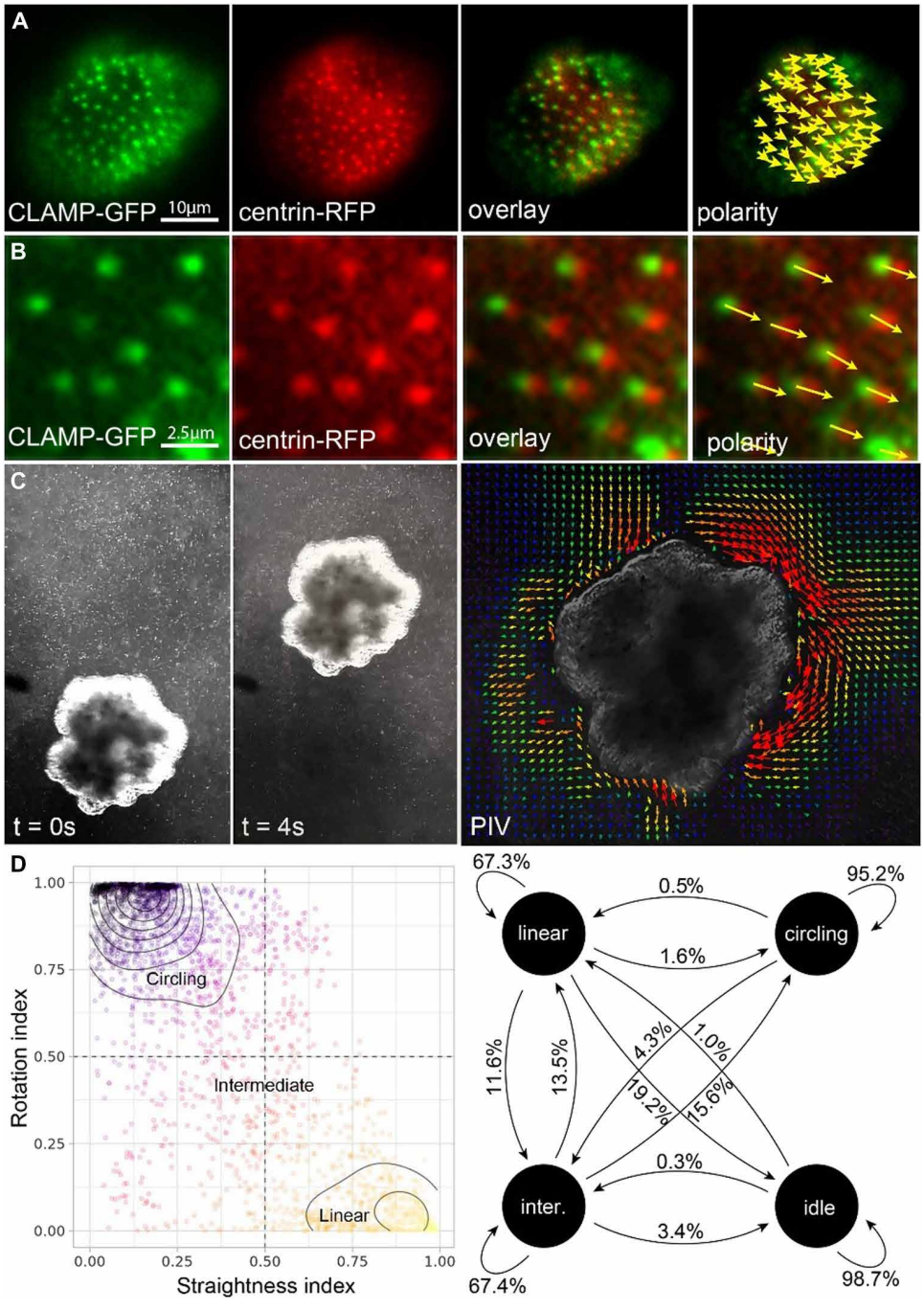

Fig. 2. Tissue-level cilia polarity produces discrete behavior states. (**A**) Within-cell cilia polarity was visualized through expression of CLAMP-GFP and centrin-RFP fusion proteins. (**B**) Magnification (4×) of the images in (A) reveals the direction of cilium orientation based on the relative positions of CLAMP and centrin protein localization (yellow arrows). (**C**) Tissue-level cilia generated flow that was visualized by recording xenobots swimming through an aqueous solution containing carmine particles under substage illumination. PIV analysis between successive video frames provides displacement vectors along the lateral surface of the xenobot during locomotion. (**D**) Cross-entropy clustering of 12 hours of xenobot tracking data broken into 30-s blocks produced three movement states: linear (yellow), circling (purple), and intermediate. A state transition probability diagram shows that idle and circling xenobots maintain their existing movement patterns, whereas those moving linearly are more likely to transition to another type of movement.

rhodamine isothiocyanate (TRITC) cubes. Of the 10 individuals imaged, 7 showed a complete lack of fluorescence in the red channel, indicating that they did not experience enough 400-nm light to photoconvert. Three individuals had strong emission at red wavelengths, revealing exposure to blue light during the 2-hour exploration period (Fig. 4, D and E). Together, these data demonstrate that engineered read/write circuitry can be easily introduced and assayed in living xenobots, allowing a subsequently retrievable record of their experience.

Xenobots can move through varied environments

To test the ability of individual xenobots to navigate varied environments, we constructed arenas of decreasing dimension ranging from completely open fields to restricted capillaries with a 580-nm inner diameter. In all cases, the xenobots were capable of locomoting through the space, although some individuals became challenged in narrow passages. In an open arena containing a debris field of variously sized carmine particles, movement was similar to the results presented above, and individuals showed varied combinations of linear and circling movement types (Fig. 5A). Reducing the size of the arena to a 1-cm-width maze, xenobots moved along the center of the channel and were observed occasionally reversing directions during the observation period (Fig. 5B). Whereas the tendency to stay in the center of the channel is likely due to the rounded nature of the floor of the maze, it is unclear what caused reversals in direction because they did not occur repeatedly at the same location or within the same individual. Within-cell and tissue-wide polarity are set up during the self-assembly phase of xenobot creation by cellular rearrangements and cannot change on short time scales. The rapid changes observed during observations could thus be due to real-time control of cilia such as changes in the beat frequency of individual multiciliated cells rather than shifts in structural polarity. As in many unicellular and multicellular organisms that use cilia for locomotion, this kind of exploratory behavior (spontaneous change in motion) can be affected by stochastic internal physiological processes and microvariation in their environment,

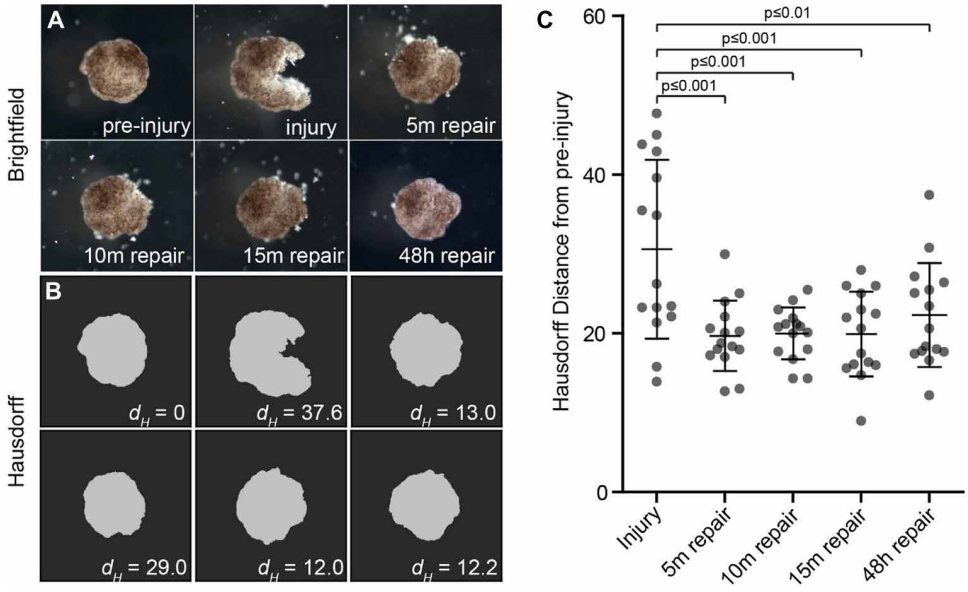

Fig. 3. Xenobots demonstrate robust repair in response to mechanical damage. (**A**) Individuals were given mechanical lacerations with surgical forceps and imaged before; immediately after; 5, 10, and15 min after injury; and after 48 hours of healing. In all cases, individuals were capable of closing the wound and resolving the injury. (**B**) To quantify repair, images were first binarized using edge detection software. The resulting images were passed through Hausdorff distance software, comparing the preinjury state with proceeding time points. (**C**) All repair time points showed significant improvement over that of the initial injury. Repeated-measures ANOVA, followed by Dunnett's post hoc comparisons. Error bars indicate ±1 SD.

such as self-generated currents in the aqueous media (which, in these experiments, contained no complex molecules, bulk flow, or gradients).

A further reduction of maze width to 2 mm resulted in frequent circling of one wall of the maze (Fig. 5C). Given the observation that most xenobots tend to exhibit elliptical movement patterns, it is likely that this behavior arises from the walls inhibiting completion of an elliptical path, which, in turn, drives the resultant directional movement. Last, individuals were placed at one end of a 2-cm capillary tube with a 580-nm inner diameter (Fig. 5D). Unexpectedly, 42% of xenobots tested (n = 12) were able to traverse the capillary end to end, and this number included some individuals that did not show movement in the open-field test. In addition, all individuals demonstrating movement successfully traversed the entire length of capillary—none became lodged or reversed directions at intermediate locations between the two ends. Together, these data reveal that xenobots can successfully traverse varied environments without having been specifically shaped or constructed to fit a given scenario, a desirable feature in many soft-bodied robotic applications.

Modeling emergent collective behavior: Particle aggregation

Beyond individual movement, cohorts of xenobots demonstrate emergent group behaviors, such as the spontaneous aggregation of particles resulting from their joint movement patterns (*11*). Here, we have further characterized this behavior by releasing multiple xenobots into arenas covered with 5 μM silicone-coated iron oxide spheres and filming a time-lapse video of subsequent movements. Over the course of 12 hours, regions of the arena were swept clean of the particles, creating piles of debris across the field (Fig. 6, A and B). The size and density of the particles here are notably larger than those used in prior work, extending the potential uses of the xenobots.

We hypothesized that the remarkable effect of their combined behaviors upon the environment could be achieved as an emergent property, not requiring feedback and active sensing/control by the bots. To investigate this possibility, we used a physics-based simulator in combination with an evolutionary algorithm to reproduce the behavior in silico using sensor-less designs. Although previous work (*11*) used similar artificial intelligence models to predict movement in cardiac-driven "walking" xenobots, accurately predicting cilia-driven movement of an individual physical xenobot presented several challenges. For example, the behavior of the swimming xenobots is not obviously determined by their geometry: Similar spherical bodies can move very differently. Even a single swimming xenobot can exhibit a complex behavioral repertoire driven by tumbling behavior along its axes rather than traveling along a single trajectory.

To overcome these barriers, we developed a graphics processing unit (GPU)–accelerated physics engine (*40*) and used it to evolve pile-making swarm behavior in simulated xenobots. This involved hundreds of thousands of simulations of swarm behavior, whereas in previous work, only a single simulation of xenobot swarm behavior was reported (*11*). Five spherical xenobot disks (each with a diameter of nine voxels and a height of seven voxels) were placed amid a 35-by-35 grid of loose voxel debris (Fig. 6C). The simulated xenobots' initially spherical bodies were shaved down by two ventral voxel layers (Fig. 6C') to increase the surface area in contact with the simulated ground plane. This stabilizes their movement and reduces the likelihood of persistent tumbling behavior in silico (a behavior that is not common in physical xenobots).

Five independent evolutionary trials were then conducted. Each trial started with its own unique set of 40 random genetic networks, yielding five champion swarms: the design that achieved the highest value of Eq. 3 below in each evolutionary trial. In addition, no movement from the swarm results in a fitness of zero. After behaving for 10 s, swarms generated by the random networks (Fig. 6D) had a mean fitness of 1098.63 ± 811.19 (SD). After 500 generations of evolutionary improvement (<48-hour wall clock time), the five champion swarms (Fig. 6E) had a mean fitness of 4278.2 ± 76.69, which is significantly better pile-making (t = −8.71966; P < 0.00001) according to the imposed objective function. This suggests that evolution did occur in silico. It also supports the hypothesis that "hard-coded" behavioral trajectories of individual xenobots, when combined together with debris under physical forces, can generate piles without sensory feedback.

Particle-gathering behavior could enable a number of useful environmental applications for xenobots in the future, especially if the size and distribution of the piles could be specified by the investigator. To assess the controllability of swimming xenobots, we performed a second set of experiments to determine whether the shape

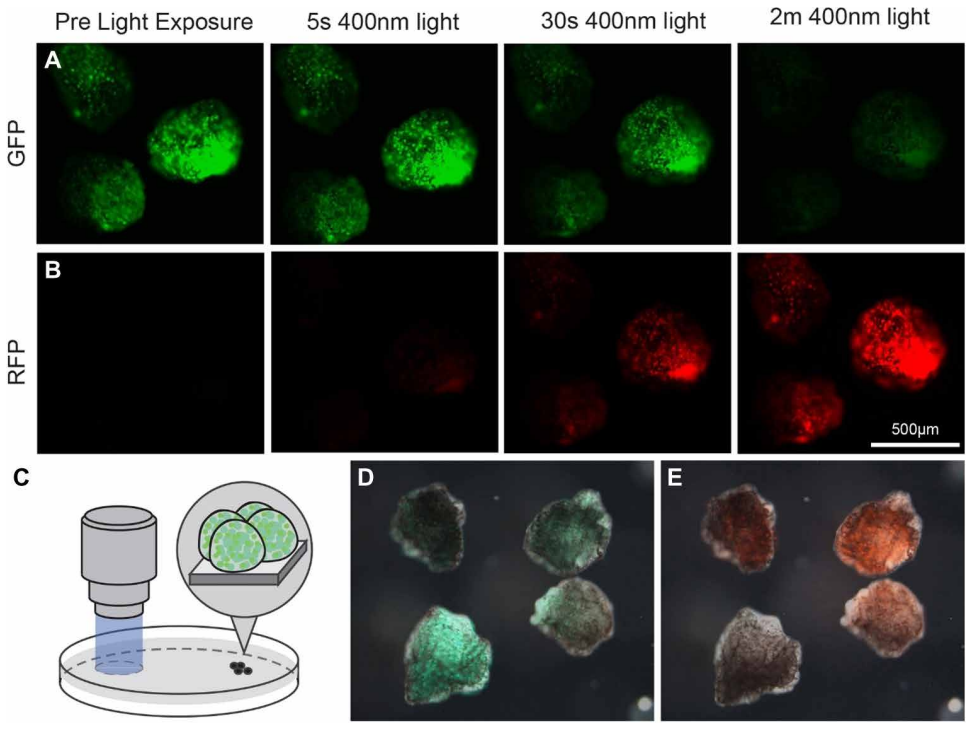

Fig. 4. Xenobots can record experience using a photoconvertible fluorescent reporter. (**A**) Xenobots injected with mRNA encoding the protein EosFP emit strong green fluorescence at 5 days of development. This signal permanently photo-converts to red when exposed to 390-nm light (**B**) due to an irreversible break in the backbone of the chromophore. (**C**) Using this reporter, xenobots were introduced into a 5-cm arena containing an illuminated spot 7 mm in diameter. After exploring the environment for 1 hour, the individuals were collected and housed in a 14°C incubator. (**D** and **E**) Two days later, fluorescent imaging revealed which xenobots moved through the blue light during their exploration of the dish.

of individual sensor-less xenobots could be designed to enhance collective particle aggregation. The experimental design was the same, except each swarm had a second genotype network (in addition to cilia forces) that determined the shape of each xenobot. Across 10 additional evolutionary trials, swarms generated from the initial set of randomly generated network pairs had a mean fitness of 687.58 ± 826.88 (SD). After 500 generations of evolutionary improvement, the five most fit swarms (one from each trial) (Fig. 6, F and G) had a mean fitness of 12,671.9 ± 3930.18, which suggests that evolution did occur ($t = -36.37944$; $P < 0.00001$). In addition, the data suggest that the mean fitness achieved with morphological change is higher than without morphological change ($t = -4.4454$; $P < 0.00033$).

It was found that all evolved swarms could be physically constructed in the real world: Xenobot morphology can be sculpted from an initially spherical body (Fig. 6, F' and F") using microsurgery tools. In a single swimming xenobot, the successful transfer of behavior from in silico to in vivo remains an open problem. Although it is challenging to predict cilia-driven movement of an individual physical xenobot, the degree to which a swarm tends to herd particles may be sufficiently determined by their shape, providing useful avenues for downstream applications in the real world.

DISCUSSION

Here, we documented the creation of xenobots, synthetic living machines derived from amphibian embryonic explants, and their ability to spontaneously exhibit collective behavior. We also outline the potential to design such swarms in the future to exaggerate these behaviors. Compared with our previously reported design method [which produced contractile-driven motion through top-down implementation of shape and tissue placement (*11*)], the xenobots reported here exhibit bottom-up emergent behaviors and generate movement through multiciliated cell propulsion. These swimming xenobots survive for up to 10 days in mild saline solution without additional energy sources and for multiple months if supplemented with cell culture medium. Movement first appeared 4 days after construction, and average velocity remained constant across the life span of the xenobot cohorts. Further, motion could be inhibited through the overexpression of NotchICD, which inhibits multiciliated cell development by driving precursors to other epidermal lineages. Together, this design method allows for the rapid generation of many mobile constructs with minimum top-down design from the investigator.

Xenobot speed and behavior remained constant across their 10-day life span, pointing to their potential for maintaining desired swarm behavior. Movement tended toward circular rotation, although arcing and linear motion were also observed less frequently. An interesting future area of study would include the enhancement of planar cell polarity patterning, enforcing specific tissue-scale cilia alignment to drive user-specified motion types. Further, given their ability to self-locomote, xenobots can move through a variety of diverse environments from open fields to narrow capillaries. These features suggest several possible downstream applications that are difficult for traditional robots, from cleaning microfluidic chambers to environmental sensing and ecologically benign remediation in natural waterways.

The ability to program rudimentary sensing and memory into xenobots was also demonstrated. Because xenobots can explore an aqueous environment, we designed a proof-of-principle system where an individual can record exposure to an environmental stimulus that can be read at a later time by an observer, using the photoconvertible reporter EosFP. After expressing the protein in xenobots through mRNA microinjection, individuals emitted strong fluorescence in green wavelengths. However, after exposure to 400-nm blue light, the reporter undergoes a permanent conformational change, shifting emission wavelengths from green to red. Using this feature, we were able to show that unsupervised xenobots could explore an environment containing an illuminated blue spot, and exposure to this light could subsequently be assessed using fluorescent microscopy. The general methodology of the approach could be readily adapted to a wide variety of scenarios, including increased/decreased sensitivity to stimuli, chemical/contaminant detection,

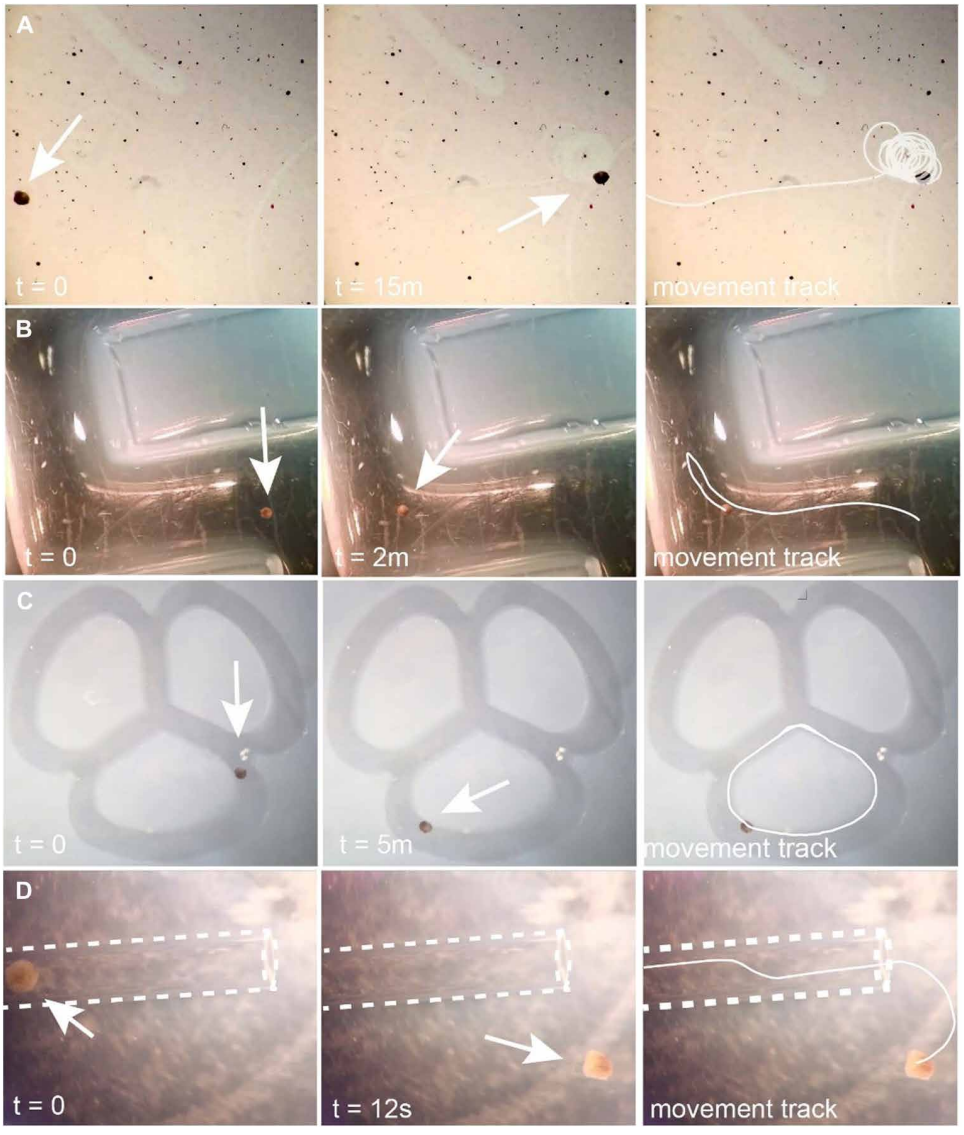

Fig. 5. Xenobots navigate diverse environments. (**A**) Xenobots were released into an open field with debris composed of carmine dye particles. Similar to prior observations, individuals demonstrate a variety of movement types, from linear motion to elliptical tracks. (**B**) In large mazes, individuals follow channels provided by the environment. (**C**) Narrow mazes begin to restrict rotational movement, resulting in individuals following edges in the arena. (**D**) In a narrow glass capillary with a 0.58-mm inner diameter, individuals can traverse the length of the tunnel and emerge from the opposite end.

bioaccumulation of target substances, release of compounds upon sensation of stimuli, multimodal recording, and nested if/then circuitry.

Unlike current robots, in which robustness must be programmed, xenobots exhibit automatic self-repair after injury. When presented with lacerations, all individuals were able to heal the wound within 15 min, and in no cases did an individual perish as a result of the injury. Tadpoles also rapidly resolve injuries resulting from mechanical damage or transplantation, revealing that, like ciliary motion, emergent capabilities of cell groups can be deployed in different ways on very different body architectures. Further, contraction at the wound site is sufficient to close minor injuries, but the mechanism behind large-scale damage repair is unknown. The ability to self-repair remains an important feature of soft-bodied robots that is difficult to achieve using synthetic materials (*41*) but emerges naturally from the biology of our constructs.

Although current xenobots do not contain specialized sense organs, they display many behaviors comparable to those observed in highly sensorized robots, including the aggregation of environmental debris. We found that xenobots can move through and push small amounts of debris, clearing regions of the arena while depositing piles of material elsewhere. To test whether this behavior could result purely from the physics of sensor-less locomoting bodies, we developed a GPU-based physics engine that could handle the computational demands of many interacting soft bodies at high mechanical resolution. Our simulation results demonstrate that it is possible to achieve the complex pile-making behavior seen in the physical xenobots without any feedback from sensors. These modeling studies also provide a framework for predicting the collective behavior of a swarm of cilia-driven physical xenobots based on their geometry, despite the difficulty of predicting cilia-driven movement of an individual physical xenobot. Such studies also suggest that machine learning methods may, in the future, automatically design the shape and tissue distribution of simulated xenobots to maximize desired collective behavior in silico, which retains that collective function when physical copies of the best designs are constructed and deployed. This seems achievable, because sim2real transference was obtained with xenobots previously, for desired individual behavior (*11*).

Last, fully biological robots differ from both robot swarms and modular robots in that they exhibit collective behavior and modularity on at least four scales. There is the xenobot swarm itself, but each individual xenobot is composed of thousands of cells, each of which is itself a complex and semiautonomous machine. Last, the intricate internal architecture of a cell houses myriad self-motile machines that build and maintain cellular integrity and function. Such multiscale structure poses unique future challenges and opportunities for altering collective function at each and all of these scales.

Together, these in vitro and in silico results provide a pipeline to move between the physical and the virtual world, where results in one environment can inform the other. For example, modeling may allow rapid testing of many parameters that would be impossible biologically because of the time and effort involved. Alternatively,

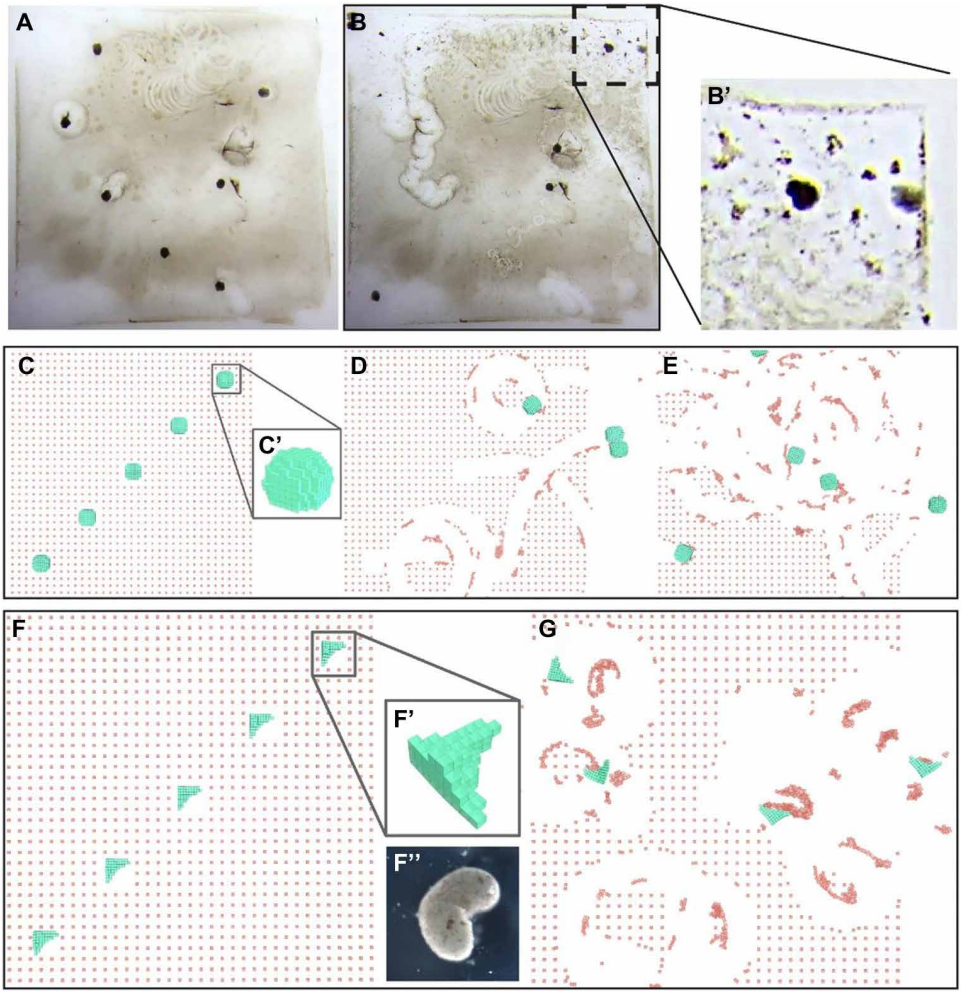

Fig. 6. Modeling collective behavior. (**A**) Six living xenobots were released into an arena covered in 5- to 10-μm silicone-coated iron oxide beads. (**B**) After 12 hours, the living xenobots cleared regions of the arena, creating piles of particles across the environment (B′). (**C**) Five simulated xenobots (green) were initially placed within a 35-by-35 grid of particulate matter (red) and collectively evolved in silico as a swarm to recapitulate a specific behavior observed in vivo: pile making. (**D**) The xenobots were identically shaped and propelled with open-loop control (no sensors were included) according to an initially random set of static cilia forces. (**E**) The simulated xenobots were "blind," but nevertheless, after 500 generations of evolution in silico, the simulated swarm exhibited dynamic coupling, complex movement trajectories, and herding behavior by pushing the initially separated debris into central piles. (**F**) The body shape of five simulated xenobots (F′) (green) was evolved in silico to aggregate particulate matter. Each individual xenobot in the swarm shares the same evolved morphology but has its own evolved cilia controller. The living xenobots in this paper have spherical bodies but can be sculpted in vitro to match the computer-generated blueprint (F″) that enhance particle aggregation in simulated xenobots (**G**).

biological experiments can provide baselines and constraints to existing models, refining them with values that are translatable to real-world scenarios for a range of downstream applications.

The computational modeling of unexpected, emergent properties at multiple scales and the apparent plasticity of cells with wild-type genomes to cooperate toward the construction of various functional body architectures offer a very potent synergy. Future work to better predict and control the structure and function of synthetic living machines could be influential to several fields. Basic evolutionary developmental biology and basal cognition can use this model to understand self-assembly of body forms and functional controllers. Moreover, existing toolkits of synthetic biology, bioelectrical signaling, and computation via cell networks offer an extremely rich space of possible living machines with useful functions including biomedicine, environmental remediation, and exploration (*42*–*46*).

MATERIALS AND METHODS

We here survey the stages of the biological construction process, computational design of simulated xenobots to exhibit a representative collective behavior, and analysis of the distinct behaviors exhibited by a swarm of xenobots performing this behavior.

Animal husbandry

All experiments were conducted using fertilized *X. laevis* embryos as donor tissue. Wild-type embryos were collected 30 min after fertilization and reared in 0.1× MMR solution (pH 7.8) at 14°C before microinjection or animal cap dissection. Experimental procedures using animals for experimental purposes were approved by the Institutional Animal Care and Use Committee and Tufts University Department of Laboratory Animal Medicine under protocol number M2020-35.

Explant culture

Xenopus animal cap explants were performed using standard methods (*47*). Briefly, fertilized embryos were raised at 14°C in 0.1× MMR (pH 7.8), until Neiuwkoop and Faber stage 9. The vitelline membrane of each embryo was removed with surgical forceps (Dumont, 11241-30 #4) before being transferred to a 1% agarose-lined petri dish containing 0.75× MMR for excision. Surgical forceps were then used to remove a circular mass of tissue from the animal-most region of each blastula embryo, after which the remainder of the embryo was removed from the dish. Each explant was then inverted and allowed to heal for 30 min to 1 hour in 0.75× MMR, allowing the tissue to ball up into a spherical mass. After healing, all the explants from each treatment were transferred to fresh 1% agarose-covered dishes containing 10 ml of 0.75× MMR and gentamicin (5 ng/μl) and cultured at 14°C until ready for use. Media was replaced three times a week to clean out cellular debris and any possible contamination.

For long-term growth studies extending beyond the normal 10-day life span, explants were raised in *Xenopus* cell culture media containing 50% Ringer's solution, 49% Leibovitz L-15 medium (Thermo Fisher Scientific, 11415064), and 1% fetal bovine serum.

Explants were placed into individual wells of a 24-well plate lined with 2% agarose and were fed with 1 ml of culture media and gentamicin (5 ng/μl). Explants were moved to new wells with fresh media three times per week to reduce the likelihood of fungal contamination.

In experiments using the K^+ inhibitor/Ca_2^+ activator barium chloride, xenobots were exposed to a 2.0 mM solution in 0.75× MMR beginning 3 to 4 hours after excision/healing and kept in the solutions throughout the remainder of the study. All pharmaceuticals were stored as stocks at 4°C, and working solutions were refreshed every 3 days.

Microinjection

All mRNA was synthesized using standard message machine kits (Life Technologies) and stored at −80°C until use. Before injection, cohorts of four-cell–stage embryos were transferred to a 3% Ficoll solution and aligned in a laser-etched petri dish. Individual embryos were then injected into each of the four cells using a pulled capillary to deliver about 500 ng of RNA in a 50-nl volume to each cell. Four cell embryos were chosen for injection over one cell because of the observation that expression tended to be more uniform at the four-cell stage. Two hours after microinjection, the embryos were washed twice in 0.1× MMR (pH 7.8), moved to fresh petri dishes, and moved to a 22°C incubator overnight. The following morning, the embryos were cleaned one final time before processing for animal cap excision. Constructs used in the current study included the multiciliated cell inhibitor NotchICD (*48*, *49*) EosFP (*39*), centrin-RFP (*35*, *36*), and CLAMP-GFP (*35*, *36*).

Immunohistochemistry

Multiciliated cell number was visualized through immunohistochemistry with the monoclonal anti-acetylated α-tubulin antibody (Sigma-Aldrich, T7451) using a protocol described previously (*50*). Cohorts of xenobots from each treatment were pooled and transferred to a 3-ml scintillation vial containing MEMFA fixative [100 mM Mops (pH 7.4), 2 mM EGTA, 1 mM $MgSO_4$, and 3.7% (v/v) formaldehyde]. Fixation proceeded for 2 hours at room temperature on a nutator, after which, the fixative was removed with a disposable pipette, and the xenobots were washed three times, 10 min per wash, in phosphate-buffered saline + 0.1% Tween 20 (PBST) and stored at 4°C until ready for processing. Processing began by blocking for 1 hour at room temperature with 10% goat serum in PBST. Samples were then rocked overnight at 4°C in monoclonal anti-acetylated α-tubulin antibody diluted at 1:1000 in PBST + 10% goat serum. After primary incubation, samples were washed three times for 15 min in PBST before a 60-min secondary incubation with Alexa Fluor 555–conjugated secondary antibody at 1:500 dilution in PBST. After secondary incubation, samples were washed three times for 15 min in PBST.

Behavioral analysis

Mazes used in behavioral tests were created from acrylic negatives and cast with 2% agarose. Each negative was affixed to the lid of a petri dish with a spot of cyanoacrylate-based adhesive and lowered into a dish containing sufficient volume of melted agarose to submerge the maze one-half of its total height. Dishes were cooled at room temperature for 1 hour before being wrapped in Parafilm and stored at 4°C until use. For glass capillary experiments, standard 1.0–mm–outer diameter, 0.5–mm–inner diameter, 4-inch-length capillaries (Sutter Instruments, BF100-50-10) were cut down to a 2 cm length using a diamond knife. Individual xenobots were then manually loaded into one end of the capillary and observed for 10 min on a stereoscope with an attached Sony IMX234 camera. In cases where movement was observed moving out of the loading area (i.e., the opposite direction of the preferred movement), the individual was rotated 180° and reloaded in the same manner. Trials were considered a success if the individual emerged from the opposite end of the capillary.

For particle aggregation and displacement experiments, a stock solution carmine dye (Sigma-Aldrich, C1022-5G) was created at a concentration of 0.01 g per 10 ml of 0.75× MMR and vortexed for 10 s. Individual working solutions were then created in 1% agarose-coated polystyrene petri dishes by diluting the stock at 1:10, again in 0.75× MMR, for a final concentration of 0.001 g per 10 ml. Dishes containing the working solution were housed under an imaging microscope and allowed to settle for 4 hours at 22°C, creating a layer of particulate dye on the surface of the dish. Silicone-coated iron oxide spheres (Ocean NanoTech, SOR-10-50) were prepared in a similar manner, although only 1 hour of settling was necessary because of the higher density of the material. PIV analysis was performed using the ImageJ iterative PIV plugin with a correlational threshold of 0.60. Individual xenobots were filmed at 30 frames/s in an aqueous environment containing carmine particles, and successive frames were extracted and processed to produce displacement vector fields.

Movement state transition probabilities

Movement states transition diagrams were produced via analysis of 12-hour tracking videos. Xenobot trajectories were extracted from the experimental videos using the trackR function in the trackR package (version 0.3.2) for R (*51*). For each position of each trajectory, the following metrics were calculated: (i) the linear distance between the current position and the immediately preceding one; (ii) the linear speed at each position, approximated as the distance moved between the current position and the immediately preceding one during the time interval between these two positions; (iii) the heading of the bot at each position, approximated as the angle between the vector formed by the current position and the immediately preceding one and that formed by the current position and the immediately following one; (iv) the angular speed of the bot at each position, approximated as the difference between the heading at the immediately preceding position and that at the current one during the time interval between the corresponding three positions required to calculate these two headings; (v) the time difference between each position.

Behavioral classification was then performed on nonoverlapping 30-s blocks of trajectory. To determine how predictable a position change was, the linear speed, heading, and angular speed were estimated at each position to predict the coordinates of the following position. The error (Euclidean distance) between the predicted coordinates and the actual coordinates was then computed. For each complete 30-s block of trajectory (i.e., a block with no missing time stamp), total error over the entire block was calculated and normalized by the total distance traveled during that block to account for the artificial error amplification caused by predicting over longer distances. All blocks were discarded that have at least one point within 0.5 mm of the arena wall to eliminate edge effects on the bots' behaviors. To separate active from inactive blocks, an automated classification method was used on the distribution of total normalized errors. A gamma mixture model with two components

was fit to the data using the expectation maximization algorithm in the REBMIX function from the rebmix package (version 2.12.0) (*52*) for R.

Recorded tracks revealed that the xenobot movement could be described as a combination of straight lines and circles (or arcs). The following two indices were defined to capture the most common path classes displayed by the bots during each block: (i) a "straightness" index computed as 1 minus the circular variance of the headings during the block (a value of 1 indicates a perfectly straight line) and (ii) a "gyration" index computed as 1 minus the circular variance of the angular speeds during the block divided by the circular variance of the angular speeds (a value of 1 indicates a trajectory following a perfect circle). To separate the trajectory blocks into categories of similar behavior, a cross-entropy clustering algorithm was used, described in (*53*), and implemented in the cec function of the CEC package (version 0.10.2) (*54*) for R. Last, to understand how the bots' behaviors are distributed relative to each other, transition probabilities between each behavioral category were estimated by calculating the proportion of times a block of a given category is followed by a block of the same or another category. The source code and full documentation for these methods can be found at (*55*).

Wound healing

To assess wound healing, individual xenobots aged 4 to 7 days after explantation were moved to fresh 1% agarose-coated petri dishes containing 0.75× MMR. Surgical forceps were used to create a mechanical laceration spanning about one-half the diameter of the individual. Images were collected before injury; directly after injury; 5, 10, and 15 min after injury; and after 48 hours of healing. Images were first processed by cropping, downsampling, and binarization. To crop the images, contours were automatically drawn on the image by traversing the boundaries of each transition between body and background pixels to find closed loops (each of which is a contour). A bounding box was then drawn around the largest contour (by area), and the rest of the image was trimmed off. Last, the cropped images were resized (downsampled) to a constant resolution (300 pixels × 300 pixels). These processed images were then assessed by comparing each time point to its initial shape using Hausdorff distance. To calculate Hausdorff distance, the image was binarized, with each pixel assigned either 1 (for pixels belonging to the body of the organism) or 0 (the background). The Hausdorff distance is the largest discrepancy between pairs of pre- and postdamage body pixel coordinates, in terms of Euclidean distance.

Formally, the Hausdorff distance for tissue type 1 is defined as

$$H = \max\{\sup_{a\in A}\inf_{b\in B} d(a,b), \sup_{b\in B}\inf_{a\in A} d(a,b)\} \quad (1)$$

where A and B are the sets of pre- and postdamage pixels, and d(a, b) is the Euclidean distance between pixels a and b. A small Hausdorff distance indicates that for every pixel before damage, there is a pixel nearby after damage, and vice versa. During repair, we measure the amount of shape change toward the predamage shape using the statistic

$$\Delta = H_{post}/H_{injury} \quad (2)$$

which is a ratio of two Hausdorff distances: one taken at recovery (numerator) and the other immediately after injury (denominator).

Because H is sensitive to rotation, H was calculated 360 times for every postdamage image, each time rotating the image by 1°. The rotation with the best match (the smallest H) was selected. Because H is sensitive to the position of the body within the frame of an image, copies of images were auto-cropped such that the edge of the design fills the frame, and H was recalculated (with 360 rotations). Final Hausdorff distances conformed to normality and were compared using a repeated-measures ANOVA, followed by Dunnett's post hoc comparison of injury values to all proceeding time points.

Imaging

Xenobot morphology was imaged using a Nikon SMZ-1500 microscope attached to a QImaging Retiga 2000R charge-coupled device (CCD) camera. Live samples were photographed in 0.75× MMR at 22°C using both overhead and substage illumination in combination with a concavity slide to keep the xenobots in view. Immunofluorescence was detected using a 4× or 10× objective and standard TRITC filter cube on an Olympus BX-61 microscope equipped with a Photometrics CoolSNAP DYNO CCD camera and CoolLED pE-300 light source. Images were captured as tiff z-stacks and combined into composite images using Metamorph software before being moved to ImageJ for analysis.

Motion tracking

Motion tracking of xenobot behavior was completed by uploading time-lapse videos into Ethovision XT v.14/15 (Noldus Information Technology). A scaled background image was uploaded before data processing to accurately set movement speeds and distance. Tracking was completed in using automated settings, and the coordinates of each xenobot position across the time lapse were then exported as an .xslv file via analysis tools. Any tracking errors were manually removed (field values left empty) in the .xslv file after the coordinates were exported from Ethovision for statistical analysis.

Modeling collective behavior

All modeling was run in voxcraft-sim (*40*), a GPU-accelerated implementation of the Voxcad environment, which has been documented previously (*56*, *57*). Xenobots are simulated by hundreds of elastic voxels (deformable cuboids), each approximating a section of tissue rather than a one-to-one voxel-to-cell representation. At each time step, the dynamics (position and motion) of every voxel can be updated in parallel across multiple independent GPU threads. Xenobots here were simulated with Young's modulus of 0.02 MPa, density of 1500 kg/m^3, 0.35 Poisson's ratio, and coefficients of static and dynamic friction of 1 and 0.5, respectively. The simulated debris were slightly stiffer (0.03 MPa), less dense (1000 kg/m^3), and had a higher coefficient of dynamic friction (0.8). The debris were made slightly adhesive to better approximate the real properties of the physical particulate matter: A persisting but breakable bond was formed between a pair of voxels if they touched and broken if the bond's stress exceeds a threshold (0.05 MPa).

The material properties of the voxels were manually adjusted for simulation speed (heavier/softer material can be stably simulated with a larger time step of numerical integration because their resonance frequency is lower than lighter/stiffer material). Each simulation consisted of 22,940 time steps (long enough to see pile-making behavior occur), with step size of 0.00044 s [low enough to ensure simulation stability; for details, see (*56*)], yielding an evaluation

period of 10 s. The aggregate (metachronal wave) force produced by a patch of beating cilia was modeled on each surface voxel as an impulse force originating at the center of the voxel and pointing in any direction in the horizontal (x,y) plane. Internal voxels inside a xenobot do not have cilia, nor do the debris. The maximal magnitude of the force was manually adjusted to ensure that the maximal speed would not cause continual tumbling behavior (which has not been observed in vivo).

A generative network (*58*) was used to genetically encode the cilia force of every surface voxel. The network takes as input the initial x,y,z position of a voxel (at simulation time $t = 0$) and outputs an impulse force for that voxel. This force is then fixed for the remainder of the evaluation period. The network is inherently biased such that when it generates the constant force for each surface voxel in the simulated swarm, voxel pairs close together in space are more likely to have similar cilia forces than a pair of initially distant voxels. This biases search toward spatial regularity. For more details, see (*59*).

An evolutionary algorithm (*60*) was used that maintains a population of 40 initially random genetic networks for 500 generations. At every generation, the population is doubled by making a randomly mutated copy of each of the 40 networks, where a mutation either adds, removes, or modifies one of the network's edges or vertices [for more details, see (*11*)]. Each network then generates cilia forces for a swarm of virtual xenobots, and the swarm's behavior is evaluated for 10 s in simulation. The fitness of a swarm (F) was measured as the number of debris voxel pairs within three voxel length units of each other (they are initialized on a grid, four voxel lengths away)

$$F = \sum_{i=1}^{1,2251,225} \sum_{j=1} d(v_i, v_j) \quad (3)$$

where v_i is the ith debris voxel (within the 35 × 35 = 1225 grid of debris), d(a,b) = 1 if dist(a,b) < 3; d(a,b) = 0 otherwise, where dist(.) is the Euclidean distance.

This objective function was intended to promote the evolution of pile-making behavior. We also investigated an alternative objective function that measured the pairwise sum of voxel distances; however, the penalty of moving debris apart resulted in no xenobot movement.

SUPPLEMENTARY MATERIALS

robotics.sciencemag.org/cgi/content/full/6/52/eabf1571/DC1

Fig. S1. Ectoderm-derived xenobots do not contain neural tissue.

Fig. S2. Xenobot life span can be extended with nutrient-rich media.

Movie S1. Time-lapse videos of synthetic organisms moving through aqueous environments.

Movie S2. Collective particle aggregation in simulated synthetic organisms.

REFERENCES AND NOTES

1. J. Yu, B. Wang, X. Du, Q. Wang, L. Zhang, Ultra-extensible ribbon-like magnetic microswarm. *Nat. Commun.* **9**, 3260 (2018).
2. A. Servant, F. Qiu, M. Mazza, K. Kostarelos, B. J. Nelson, Controlled in vivo swimming of a swarm of bacteria-like microrobotic flagella. *Adv. Mater.* **27**, 2981–2988 (2015).
3. H. Xie, M. Sun, X. Fan, Z. Lin, W. Chen, L. Wang, L. Dong, Q. He, Reconfigurable magnetic microrobot swarm: Multimode transformation, locomotion, and manipulation. *Sci. Robot.* **4**, eaav8006 (2019).
4. G. Adam, S. Chowdhury, M. Guix, B. V. Johnson, C. Bi, D. Cappelleri, Towards functional mobile microrobotic systems. *Robotics* **8**, 69 (2019).
5. M. Soreni-Harari, R. St. Pierre, C. McCue, K. Moreno, S. Bergbreiter, Multimaterial 3D printing for microrobotic mechanisms. *Soft Robot.* **7**, 59–67 (2020).
6. C. C. J. Alcântara, S. Kim, S. Lee, B. Jang, P. Thakolkaran, J.-Y. Kim, H. Choi, B. J. Nelson, S. Pané, 3D fabrication of fully iron magnetic microrobots. *Small* **15**, e1805006 (2019).
7. E. Avci, M. Grammatikopoulou, G.-Z. Yang, Laser-printing and 3D optical-control of untethered microrobots. *Adv. Opt. Mater.* **5**, 1700031 (2017).
8. Q. Wang, L. Yang, J. Yu, P. W. Y. Chiu, Y.-P. Zheng, L. Zhang, Real-time magnetic navigation of a rotating colloidal microswarm under ultrasound guidance. *IEEE Trans. Biomed. Eng.* **67**, 3403–3412 (2020).
9. I. R. Bruss, S. C. Glotzer, Curvature-induced microswarming. *Soft Matter* **13**, 5117–5121 (2017).
10. X. Dong, M. Sitti, Controlling two-dimensional collective formation and cooperative behavior of magnetic microrobot swarms. *Int. J. Robot. Res.* **39**, 617–638 (2020).
11. S. Kriegman, D. Blackiston, M. Levin, J. Bongard, A scalable pipeline for designing reconfigurable organisms. *Proc. Natl. Acad. Sci. U.S.A.* **117**, 1853–1859 (2020).
12. C. Anderson, C. D. Stern, Organizers in development. *Curr. Top. Dev. Biol.* **117**, 435–454 (2016).
13. A. Bongso, M. Richards, History and perspective of stem cell research. *Best Pract. Res. Clin. Obstet. Gynaecol.* **18**, 827–842 (2004).
14. C. B. Kimmel, R. M. Warga, T. F. Schilling, Origin and organization of the zebrafish fate map. *Development* **108**, 581–594 (1990).
15. L. Dale, J. M. Slack, Fate map for the 32-cell stage of *Xenopus laevis*. *Development* **99**, 527–551 (1987).
16. Y. Hatada, C. D. Stern, A fate map of the epiblast of the early chick embryo. *Development* **120**, 2879–2889 (1994).
17. A. Redkar, M. Montgomery, J. Litvin, Fate map of early avian cardiac progenitor cells. *Development* **128**, 2269–2279 (2001).
18. R. Falk, N. Orevi, B. Menzl, A fate map of larval organs of *Drosophila* and preblastoderm determination. *Nat. New Biol.* **246**, 19–20 (1973).
19. R. Woodrick, P. R. Martin, I. Birman, F. B. Pickett, The *Arabidopsis* embryonic shoot fate map. *Development* **127**, 813–820 (2000).
20. G. Rossi, A. Manfrin, M. P. Lutolf, Progress and potential in organoid research. *Nat. Rev. Genet.* **19**, 671–687 (2018).
21. B. Zhang, A. Korolj, B. F. L. Lai, M. Radisic, Advances in organ-on-a-chip engineering. *Nat. Rev. Mater.* **3**, 257–278 (2018).
22. J. H. Sung, Y. I. Wang, N. N. Sriram, M. Jackson, C. Long, J. J. Hickman, M. L. Shuler, Recent advances in body-on-a-chip systems. *Anal. Chem.* **91**, 330–351 (2019).
23. J. Mustard, M. Levin, Bioelectrical mechanisms for programming growth and form: Taming physiological networks for soft body robotics. *Soft Robot.* **1**, 169–191 (2014).
24. S.-J. Park, M. Gazzola, K. S. Park, S. Park, V. Di Santo, E. L. Blevins, J. U. Lind, P. H. Campbell, S. Dauth, A. K. Capulli, F. S. Pasqualini, S. Ahn, A. Cho, H. Yuan, B. M. Maoz, R. Vijaykumar, J.-W. Choi, K. Deisseroth, G. V. Lauder, L. Mahadevan, K. K. Parker, Phototactic guidance of a tissue-engineered soft-robotic ray. *Science* **353**, 158–162 (2016).
25. C. Cvetkovic, R. Raman, V. Chan, B. J. Williams, M. Tolish, P. Bajaj, M. S. Sakar, H. H. Asada, M. T. A. Saif, R. Bashir, Three-dimensionally printed biological machines powered by skeletal muscle. *Proc. Natl. Acad. Sci. U.S.A.* **111**, 10125–10130 (2014).
26. B. J. Williams, S. V. Anand, J. Rajagopalan, M. T. A. Saif, A self-propelled biohybrid swimmer at low Reynolds number. *Nat. Commun.* **5**, 3081 (2014).
27. V. Webster-Wood, F. Young, J. M. Patel, G. N. Scariano, O. Akkus, U. A. Gurkan, H. J. Chiel, R. D. Quinn, 3D-printed biohybrid robots powered by neuromuscular tissue circuits from *Aplysia californica*, in *Conference on Biomimetic and Biohybrid Systems* (Springer, 2017), pp. 475–486.
28. B. C. Gallagher, A. M. Hainski, S. A. Moody, Autonomous differentiation of dorsal axial structures from an animal cap cleavage stage blastomere in *Xenopus*. *Development* **112**, 1103–1114 (1991).
29. J. Green, The animal cap assay. *Methods Mol. Biol.* **127**, 1–13 (1999).
30. S. Sokol, D. A. Melton, Pre-existent pattern in *Xenopus* animal pole cells revealed by induction with activin. *Nature* **351**, 409–411 (1991).
31. H. L. Sive, R. M. Grainger, R. M. Harland, Animal cap isolation from *Xenopus laevis*. *Cold Spring Harb Protoc* **2007**, pdb.prot4744 (2007).
32. F. Keijzer, M. van Duijn, P. Lyon, What nervous systems do: Early evolution, input-output, and the skin brain thesis. *Adapt. Behav.* **21**, 67–85 (2013).
33. F. Baluška, M. Levin, On having no head: Cognition throughout biological systems. *Front. Psychol.* **7**, 902 (2016).
34. E. M. Eisenstein, Advances in behavioral biology v. 13, in *Aneural Organisms in Neurobiology* (Plenum Press, 1975), p. vii, 145 p.
35. E. Silva, E. Betleja, E. John, P. Spear, J. J. Moresco, S. Zhang, J. R. Yates III, B. J. Mitchell, M. R. Mahjoub, Ccdc11 is a novel centriolar satellite protein essential for ciliogenesis and establishment of left-right asymmetry. *Mol. Biol. Cell* **27**, 48–63 (2016).
36. M. E. Werner, B. J. Mitchell, Using *Xenopus* skin to study cilia development and function. *Methods Enzymol.* **525**, 191 (2013).

37. B. Mitchell, J. L. Stubbs, F. Huisman, P. Taborek, C. Yu, C. Kintner, The PCP pathway instructs the planar orientation of ciliated cells in the *Xenopus* larval skin. *Curr. Biol.* **19**, 924–929 (2009).
38. L. N. Vandenberg, D. S. Adams, M. Levin, Normalized shape and location of perturbed craniofacial structures in the *Xenopus* tadpole reveal an innate ability to achieve correct morphology. *Dev. Dyn.* **241**, 863–878 (2012).
39. J. Wiedenmann, S. Ivanchenko, F. Oswald, F. Schmitt, C. Rocker, A. Salih, K.-D. Spindler, G. U. Nienhaus, EosFP, a fluorescent marker protein with UV-inducible green-to-red fluorescence conversion. *Proc. Natl. Acad. Sci. U.S.A.* **101**, 15905–15910 (2004).
40. S. Liu, D. Matthews, S. Kriegman, J. Bongard, Voxcraft-sim, a GPU-accelerated voxel-based physics engine (2020); 10.5281/zenodo.3835152, https://github.com/voxcraft/voxcraft-sim.
41. R. A. Bilodeau, R. K. Kramer, Self-healing and damage resilience for soft robotics: A review. *Front. Robot. AI* **4**, 48 (2017).
42. A. Urrios, J. Macia, R. Manzoni, N. Conde, A. Bonforti, E. de Nadal, F. Posas, R. Solé, A synthetic multicellular memory device. *ACS Synth. Biol.* **5**, 862–873 (2016).
43. R. Solé, D. R. Amor, S. Duran-Nebreda, N. Conde-Pueyo, M. Carbonell-Ballestero, R. Montañez, Synthetic collective intelligence. *Biosystems* **148**, 47–61 (2016).
44. S. Manicka, M. Levin, The cognitive lens: A primer on conceptual tools for analysing information processing in developmental and regenerative morphogenesis. *Philos. Trans. R. Soc. Lond. Ser. B Biol. Sci.* **374**, 20180369 (2019).
45. S. Manicka, M. Levin, Modeling somatic computation with non-neural bioelectric networks. *Sci. Rep.* **9**, 18612 (2019).
46. S. Toda, L. R. Blauch, S. K. Y. Tang, L. Morsut, W. A. Lim, Programming self-organizing multicellular structures with synthetic cell-cell signaling. *Science* **361**, 156–162 (2018).
47. T. Ariizumi, S. Takahashi, T.-c. Chan, Y. Ito, T. Michiue, M. Asashima, Isolation and differentiation of *Xenopus* animal cap cells. *Curr. Protoc. Stem Cell Biol.* **Chapter 1**, Unit 1D 5 (2009).
48. D. A. Wettstein, D. L. Turner, C. Kintner, The *Xenopus* homolog of *Drosophila* suppressor of hairless mediates Notch signaling during primary neurogenesis. *Development* **124**, 693–702 (1997).
49. J. L. Stubbs, L. Davidson, R. Keller, C. Kintner, Radial intercalation of ciliated cells during *Xenopus* skin development. *Development* **133**, 2507–2515 (2006).
50. D. Blackiston, L. N. Vandenberg, M. Levin, High-throughput *Xenopus laevis* immunohistochemistry using agarose sections. *Cold Spring Harb Protoc* **2010**, pdb.prot5532 (2010).
51. S. Garnier, trackR: Simple video tracking software (2020); https://swarm-lab.github.io/trackR/.
52. B. Panić, J. Klemenc, M. Nagode, Improved initialization of the EM algorithm for mixture model parameter estimation. *Sci China Ser A Math* **373**, (2020).
53. J. Tabor, P. Spurek, Cross-entropy clustering. *Pattern Recogn.* **47**, 3046–3059 (2014).
54. K. Kamieniecki, P. Spurek, CEC: Cross-entropy clustering; https://CRAN.R-project.org/package=CEC.
55. D. Blackiston, E. Lederer, S. Kriegman, S. Garnier, J. Bongard, M. Levin, Support material for "A New Cellular Platform for the Development of Synthetic Living Machines," *Github* (2021); http://dx.doi.org/10.5281/zenodo.4435617.
56. J. Hiller, H. Lipson, Dynamic simulation of soft multimaterial 3d-printed objects. *Soft Robot.* **1**, 88–101 (2014).
57. J. Hiller, H. Lipson, Automatic design and manufacture of soft robots. *IEEE Trans. Robot.* **28**, 457–466 (2011).
58. K. O. Stanley, Compositional pattern producing networks: A novel abstraction of development. *Genet. Program Evolvable Mach.* **8**, 131–162 (2007).
59. N. Cheney, R. MacCurdy, J. Clune, H. Lipson, in *Proceedings of the 15th Annual Conference on Genetic and Evolutionary Computation* (2013), pp. 167–174.
60. M. Schmidt, H. Lipson, in *Genetic Programming Theory and Practice VIII* (Springer, 2011), pp. 129–146.

Funding: This research was sponsored by the Defense Advanced Research Projects Agency (DARPA) under Cooperative Agreement number HR0011-180200022, the Lifelong Learning Machines program from DARPA/MTO. The content of the information does not necessarily reflect the position or policy of the government, and no official endorsement should be inferred. Approved for public release; distribution is unlimited. This research was also supported by the Allen Discovery Program through The Paul G. Allen Frontiers Group (12171).
Author contributions: D.B., E.L., S.K., J.B., and M.L. conceived and designed the research questions. D.B., E.L., and S.K. performed all experiments. D.B., E.L., S.K., and S.G. analyzed data. D.B., E.L., S.K., S.G., J.B., and M.L. wrote the manuscript. **Competing interests:** A patent application (Engineered Multicellular Organisms—U.S. provisional patent application 63/136,564; international application PCT/US2021/013105) has been filed by M.L. and D.B. The other authors declare that they have no competing interests. **Data and materials availability:** The software used in this paper is covered by the Creative Commons License. Link to code base for all simulation: https://zenodo.org/record/3835152#.YD0GsxNKg6g. Link to code base for all analysis: https://swarm-lab.github.io/trackR. All other data needed to evaluate the conclusions of this paper are available in the paper or the Supplementary Materials.

Submitted 7 October 2020
Accepted 8 March 2021
Published 31 March 2021
10.1126/scirobotics.abf1571

Citation: D. Blackiston, E. Lederer, S. Kriegman, S. Garnier, J. Bongard, M. Levin, A cellular platform for the development of synthetic living machines. *Sci. Robot.* **6**, eabf1571 (2021).

Science Robotics

A cellular platform for the development of synthetic living machines

Douglas Blackiston, Emma Lederer, Sam Kriegman, Simon Garnier, Joshua Bongard and Michael Levin

Sci. Robotics **6**, eabf1571.
DOI: 10.1126/scirobotics.abf1571